CIRP Journal of Manufacturing Science and Technology 28 (2020) 38–51

Contents lists available at ScienceDirect

CIRP Journal of Manufacturing Science and Technology

journal homepage: www.elsevier.com/locate/cirpj

Synergistic approaches to ultra-precision high performance cutting

Lars Schönemann[a,d,*], Daniel Berger[a], Timo Dörgeloh[a], Oltmann Riemer[a], Ekkard Brinksmeier[a,d], Rudolf Krüger[b], Per Schreiber[b], Berend Denkena[b], Johannes Hochbein[c], Nasrin Parsa[c], Christian Schenck[c,d], Bernd Kuhfuß[c,d]

[a] Leibniz Institute for Materials Engineering IWT, Laboratory for Precision Machining LFM, Badgasteiner Straße 2, 28359 Bremen, Germany
[b] Leibniz University Hannover, Institute of Production Engineering and Machine Tools IFW, An der Universität 2, 30823 Garbsen, Germany
[c] University of Bremen, Bremen Institute for Mechanical Engineering, Badgasteiner Straße 1, 28359 Bremen, Germany
[d] University of Bremen, MAPEX Center for Materials and Processes, Germany

ARTICLE INFO

Article history:
Available online 19 February 2020

Keywords:
Diamond milling
High speed cutting
Precision balancing
Tool alignment
Eletromagnetic linear guide
Model based precision controls

ABSTRACT

Diamond milling allows for the flexible production of optical and high precision parts, but suffers from poor setup and production speeds. This paper presents recent advances that aim towards achieving high performance (HPC) and high speed cutting (HSC) in ultra-precision machining. After a short introduction, the benefits of high speed cutting for both metals and brittle-hard materials are shown. Thereafter, novel mechatronic devices are presented that enable an automated balancing of the applied air bearing spindles and the application of multiple diamond tools on one tool holder and by thus, contribute to HPC. These developments are supplemented by a novel linear guiding system based on electromagnatic levitation that, along with a dedicated model-based control system, enables fast and precise movements of the machine tool. After presenting the recent developments in detail, their synergistic performance is assessed and an outlook to future developments is given.

Introduction

Ultra-precision machining with diamond cutting tools has been known for decades for its usability in generating metal optical surfaces for technical mirrors and molds [1]. Of all applicable processes, diamond milling offers the highest flexibility in terms of machining highly complex freeform shapes [2] and structures [3]. However, Brecher et al. have determined the surface generation rate of a typical diamond milling process to be only about 2.5 mm^2 min^{-1} [2]. The generation of a complex optical part easily exceeds hours or even days [3,4]. Despite the versatility of ultra-precision machining processes, their economic efficiency is limited [5]. Some reasons will be briefly discussed here:

First of all, diamond as cutting tool material is susceptible to catastrophic tool wear when used on steel or other iron-based substrates [6] and is therefore mainly used on copper, aluminum, brass or electroless nickel. The excessive tool wear may be counteracted by using vibration assisted machining [7] or by a chemical treatment of the workpiece surface and subsurface layer [8]. Some of these technologies have found their way into production use. Especially elliptical vibration is frequently used for cutting molds for optical devices. However, this technique cannot be applied for high speed cutting applications, as the maximum vibration frequency is limited.

Secondly, due to the precision required for mirror surfaces, deterministic cutting conditions are essential to achieve a typical surface roughness of $Sa < 10$ nm and a form accuracy of $PV < 100$ nm. Even small vibrations may deteriorate the achievable roughness [9,10], while tool setting, i.e. undefined tool nose or swing radii, has an impact on the form accuracy (see [11] for turning, [12,13] for milling). Diamond milling is conducted as a fly-cutting operation, i.e. using a single diamond cutting edge [14], ensuring a defined swing radius of the tool. However, having only a single cutting edge engaged to the workpiece severely limits the applicable feed rate.

Moreover, circumferential milling tools for fly-cutting often feature comparably large swing radii of $r_{fly} = 20$ mm up to 60 mm [15], 95 mm or even larger [9]. Consequently, the rotation of such a fly-cutter may generate significant inertial forces and thus dynamic disturbances [10]. In order to minimize these vibrations, fly-cutting operations are conducted at limited spindle speeds of $n = 1000\ min^{-1}$ (e.g. [16]) to 5000 min^{-1} (e.g. [10,17]). Yet, even the slightest unbalance has to be compensated at these speeds, considering that air bearings are typically used for ultra-precision

* Corresponding author at: Leibniz Institute for Materials Engineering IWT, Laboratory for Precision Machining LFM, Badgasteiner Straße 2, 28359 Bremen, Germany.
E-mail address: schoenemann@iwt.uni-bremen.de (L. Schönemann).

https://doi.org/10.1016/j.cirpj.2019.12.001

machining [18,19]. To ensure a safe operation and to minimize dynamic distortions, the spindles are balanced to a ISO balancing grade $< G0.04$ [20]. As there are no automated procedures to achieve this goal, balancing an ultra-precision spindle is a tedious and time-consuming manual task in which weight is added at specific points of the rotor until a satisfying balance can be assured.

The UP-HPC approach

The deficits of ultra-precision machining in terms of economic efficiency can be overcome by a simple measure: more speed. More speed in cutting, more material removed in less amount of time and more effective setup of the machine tool. This paper will present recent findings of the German Research Unit FOR1845 "Ultra-Precision High Performance Cutting" (UP-HPC) that deals with several aspects of this topic (see Fig. 1).

High speed cutting (HSC) or high performance cutting (HPC) has been applied in conventional machining for several decades [21]. It has been previously shown that these techniques not only increase the economic efficiency of milling processes, but also positively influence the material removal mechanisms [22]. This also applies to micro milling [23]. This paper will show the recent findings in applying high speed cutting in ultra-precision milling and how this affects the material removal mechanisms for diamond cutting both ductile and brittle materials (Section "High speed cutting in diamond milling").

Increasing the spindle speed requires time-consuming balancing procedures. For achieving a sufficient balancing grade, tiny oscillations of the rotor have to be detected and compensation masses have to be determined [24,25,19]. Further, these masses must be accurately placed at their respective locations on the rotor. As the required masses get smaller with better balancing grades, the manual positioning becomes extremely difficult. Thus, the latest developments for automated ultra-precision unbalance measurement and compensation are presented here (Section "Ultra-precision balancing of high speed air bearing spindles").

Without being able to apply more than one cutting edge on the same tool holder, the efficiency of diamond milling is limited. Adding more cutting edges to the milling tool, however, requires a tool setting mechanism to compensate for the deviation in swing radius. Here, a novel mechanism based on thermal expansion is shown that enables tool setting during the milling procedure and yet does not introduce additional mass and volume to the tool holder (Section "Improving the eciency of diamond milling by applying additional cutting edges").

Achieving high cutting speeds allows for higher feed velocities when the same surface roughness shall be achieved. Here, common ultra-precision guides are limited: as they are designed for pure precision, their maximum velocity normally does not exceed 1000 mm min^{-1}. In this publication, a novel magnetic guide is presented that allows higher feed rates with the precision required for machining optical surfaces (Section "Increasing the feed velocity using electromagnetic levitation technology").

While additional speed is definitely necessary for more economic diamond milling, the precision of the tool path cannot be disregarded. Operating spindle and feed axes at higher speed therefore requires sophisticated control techniques. These have been developed within the FOR1845 and recent findings will be presented in this paper (Section"Dedicated UP-HPC control and metrology systems for added performance").

Last but not least, having individual measures to improve diamond milling is not enough. An economic process rather requires a synergistic approach which combines all the techniques presented here. Thus, the final part of this paper presents a common test stand which is designed to prove the viability of all developments (Section "Synergistic application of proposed techniques").

High speed cutting in diamond milling

High speed cutting of ductile materials

The application of very high cutting speeds ($v_c \geq 2000$ m min^{-1}) while diamond machining of non-ferrous, soft metals, such as OFHC copper, brass CuZn39Pb3, aluminum AlMg5 and electroless nickel was researched [26]. The investigations have been focused on three main aspects

1 the transition to adiabatic shearing,
2 the evolution of tool wear and
3 the surface finish.

Adiabatic shearing, caused by thermal softening of the machined material, leads to reduced heat transfer into the workpiece, reduced mechanical stresses and improved surface finish during conventional high speed cutting [22]. Consequently, reaching this status is desirable.

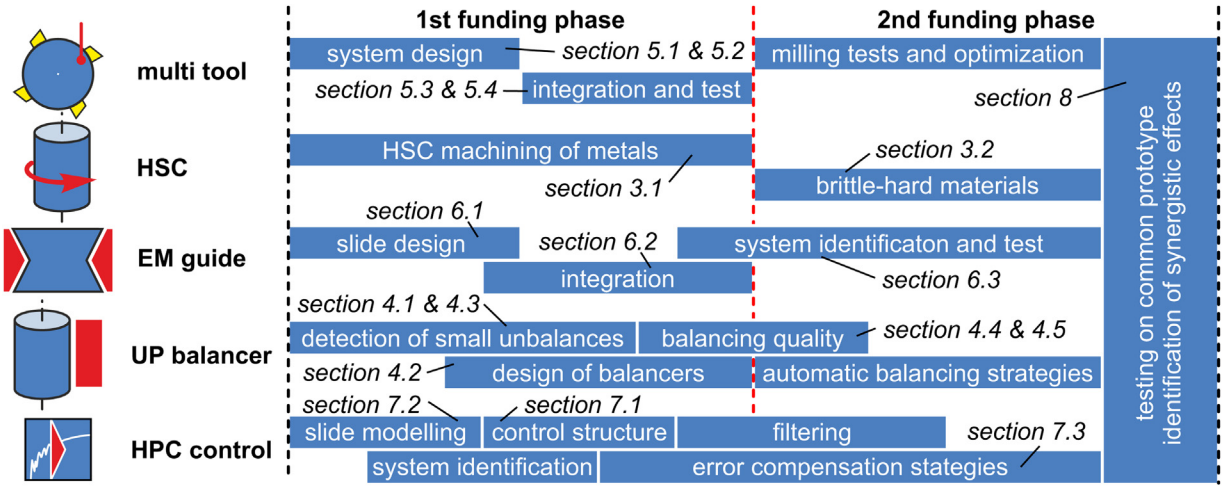

Fig. 1. Approaches of the Research Unit FOR1845 for achieving Ultra-Precision High Performance Cutting presented in this paper.

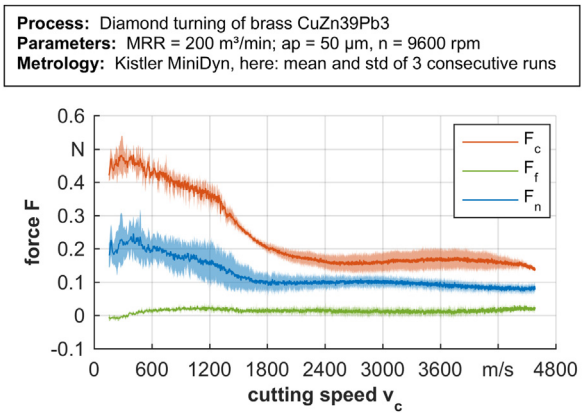

Fig. 2. Measured cutting forces vs cutting speed for diamond turning of brass CuZnPb3.

Fig. 2 shows the process forces, i.e. cutting force F_c, feed force F_f and thrust force F_n, for the machining of brass CuZnPb3. The presence of a sudden drop of the cutting force F_c is notable at a cutting speed of around 1320 m min^{-1}, indicating the transition to adiabatic shearing. This transition point occurs at different critical cutting speeds for each machined material. Other parameters influencing the transition are cutting edge radius (forces measured when applying tools with large radii do not exhibit any transition point), tool material and depth of cut.

The surface finish was investigated by measuring the step heights at grain boundaries. Step heights varied between 8 and 25 nm for ordinary cutting speeds and between 4 and 14 nm for high cutting speeds when machining OFHC copper. The better surface finish supports the hypothesis of the presence of adiabatic shearing.

Interestingly, the abrasive tool wear (flank wear) decreased with increasing cutting speed, when referring to a constant contact length. Chemical wear was also investigated and showed the same tendency. The reduced wear was explained by the very short contact times while HSC compared to ordinary cutting speeds. Additionally, reduced mechanical stresses through adiabatic shearing result in lower tool wear.

Cutting mechanics for high speed diamond milling of brittle-hard materials

The machining of brittle-hard materials with a defined cutting edge is mostly conducted to achieve defect-free and smooth surfaces. In fact, much research has been spent on ductile-regime machining, which allows a shear mode removal of the surface layer and ensures that cracks do not exceed the height of the removed layer [27].

Recent studies on ductile machining of brittle-hard materials with defined cutting edge have concentrated on modeling and simulation of crack-free milling of glass [28] and tungsten carbide [29]. Also, diamond machining of monocrystalline germanium [30] or also potassium di-hydrogen phosphate (KDP) crystals as nonlinear optical materials [31] come into focus. These studies have in common than conventional cutting speeds are applied within the experiments.

A negative rake angle entails hydrostatic pressure in the contact zone and thus increases the critical chip thickness, which enhances shear mode machining while applying conventional cutting speeds. High speed cutting does also increase the critical chip thickness due to higher temperatures and an accompanying hardness decrease in the contact zone. Thus, a beneficial influence on the machined surfaces was expected.

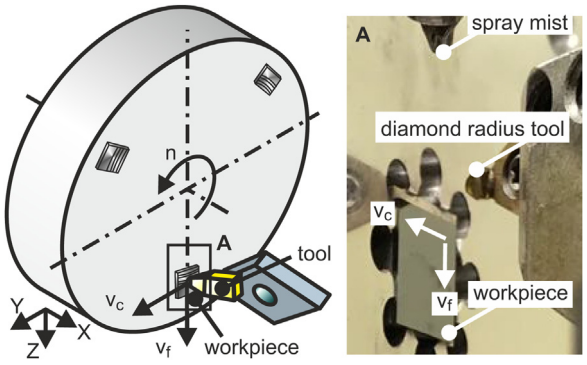

Fig. 3. Experimental setup for off-axis diamond turning of monocrystalline silicon.

Table 1
Machining, tool and workpiece parameters.

Machining	
Strategy	Machining of optical flats
Cutting speed v_c	400/4000 m min^{-1}
Feed f	5 µm
Rake angle γ	−30°
Depth of cut a_p	3 µm
Tool	
Cutting material	Single-crystal diamond
Corner radius r_ε	0.76 mm
Cutting edge radius r_β	150 nm
Workpiece	
Material	Monocrystalline silicon
Crystal orientation	(100)/(110)/(111)
Geometry	10 × 10 × 0.5 mm

Therefore, high speed cutting of brittle-hard materials was performed by off-axis diamond turning on monocrystalline silicon in this work. The critical chip thickness for crystal orientations (100), (110) and (111) was determined by machining plane surfaces for conventional and high cutting speeds. The experimental setups for turning and milling are shown in Fig. 3. The varied parameters are given in Table 1.

Process forces were measured by a force dynamometer (Kistler Type 9119AA2) on the tool side with a sampling rate of 20 kHz for the slower cutting speed and 50 kHz for $v_c = 4000$ m min^{-1}. Because the natural frequency of the setup and the applied filtering have to be taken into account when determining force values, the natural frequency was experimentally determined by using an impulse hammer (Kistler Type 9722A) and a triaxial acceleration sensor (Kistler Type 8764B). Resulting natural frequencies were 2.8 kHz for the X- and Y-axis and 3.8 kHz for the Z-axis. It is recommended by Kistler to use only one third of these frequencies for filtering the force signals. Consequently, a 1st order Butterworth filter was applied with cutoff frequencies of 0,93 kHz for the X- and Y-axis (F_p and F_c) and 1.3 kHz for the Z-axis (F_f). The results in Fig. 4 show both the filtered and the unfiltered forces. Although a reduction in cutting forces is discernible after filtering, this has to be attributed to the filter characteristics and the lack of datapoints for the higher cutting speed. The unfiltered values show similar peak heights for the cutting force.

Nevertheless, the surface roughness was reduced by applying high cutting speeds (Fig. 5). Especially for the crystal orientation (100), a significant reduction from 12.5 to 2.1 nm was determined only by increasing the cutting speed from 400 to 4000 m min^{-1}. For the other machined crystal orientations, surface roughness was in a similar range.

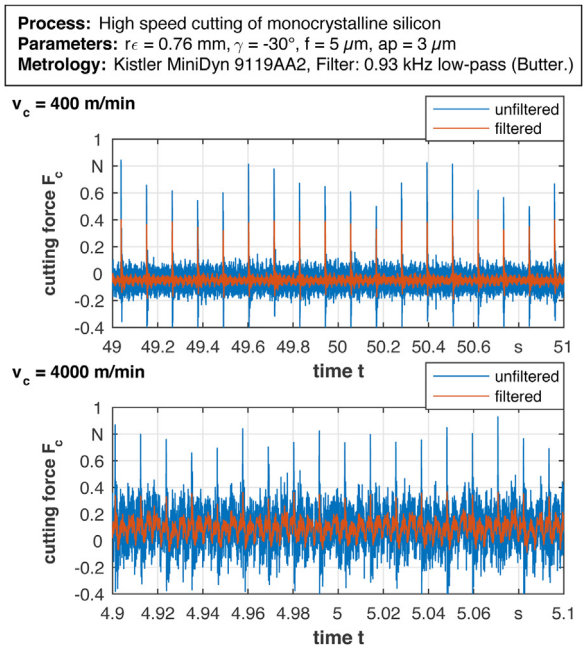

Fig. 4. Cutting forces for the machining of monocrystalline silicon (100) with low and high cutting speed.

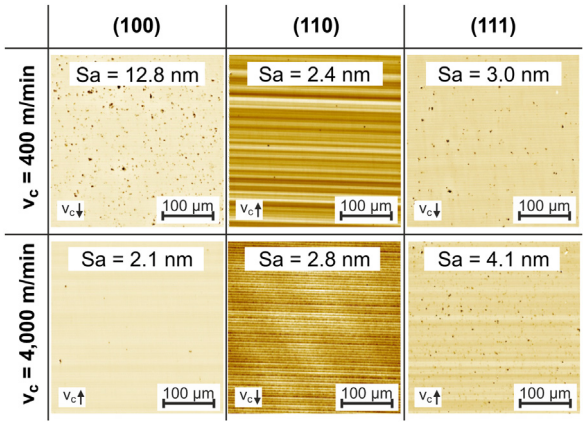

Fig. 5. Influence of high cutting speeds on surface topographies of different crystal orientations with a rake angle of $\gamma = -30^{\circ}$ and a feed of $f = 5\,\mu m$.

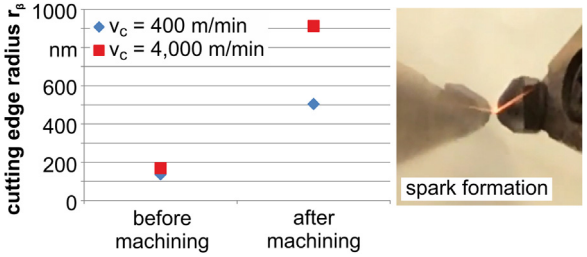

Fig. 6. Dependence of the tool wear (changing of cutting edge radius) on cutting speed and annealing color on the rake face, causing higher tool wear for high cutting speeds.

Those findings can be explained by the observations made at high speed cutting, when high temperatures occurred. Annealing colors could be spotted on the rake face of the tool, as shown in Fig. 6 (right). Comparing this with a table for the emission of electromagnetic radiation (incandescence), temperatures were estimated with 950 to 1000 °C. These temperatures lead to a hardness decrease of silicon in the shear zone with a magnitude of 10 [32]. The decrease of hardness is accompanied by an indirect increase of the critical chip thickness d_c, which is a material based parameter and can be calculated by the following Eq. (1), which considers the Young's modulus E, the specific cutting force K_c and the Vickers hardness H of the material [27]:

$$d_c \propto \frac{E}{H} \cdot \left(\frac{K_c}{H}\right)^2 \tag{1}$$

In summary, the ductile machining of brittle-hard materials is improved by high cutting speeds. A drawback is the thermal stability of diamond, which is between 700 and 800 °C. Thus, this is lower than the temperatures in the contact zone during machining and results in higher tool wear, which was measured by AFM. The determined values for the cutting edge radius before and after machining are shown in Fig. 6 (left).

Ultra-precision balancing of high speed air bearing spindles

The use of high rotational speeds is a challenge for setting up diamond fly-cutting due to a relatively large rotating mass, i.e. the tool holder, due to the quadratic influence of the angular velocity Ω on the centrifugal force F_{cen}. This leads to a significant reduction of the permissible residual specific unbalance e_{per} to achieve the same rotor balancing grade G (see Eq. (2)) with increasing rotational speed [33]:

$$G = e_{per} \cdot \Omega = \text{const.}, \text{ expressed in mm s}^{-1} \tag{2}$$

Taking the specific load constraints of air bearings into account, the required balancing grade is assumed to be G0.064, which is close to the factory balance quality [34]. This value follows the progression of the ISO standard below the current minimum of G0.16 and results in $e_{per} \approx 0.03\,\text{g mm kg}^{-1}$ at $n = 20,000\,\text{min}^{-1}$. For the machine setup of this research work, a rotor mass of $m_{rot} = 4.5\,\text{kg}$ and a compensation radius of $r_{com} = 65\,\text{mm}$ is assumed, which leads to a tolerable unbalance mass of $m_{per} \approx 2.08$ mg (see Eq. (3)).

$$m_{per} = \frac{e_{per} \cdot m_{rot}}{r_{com}} \tag{3}$$

The manual setting of such low masses is tedious and time consuming if not impossible to achieve. Thus, two balancing systems have been developed to improve the achievable balancing grade and to reduce the setup times. System one (see [35]) is based on mass removal at predefined positions for generating a counterbalance and system two (see [36]) enables a circumferential mass redistribution. Both systems are regarded as suitable for ultra-precise balancing and will be presented in the following investigations.

Automated balancing systems

The first balancing system, shown in Fig. 7, is inspired by conventional balancing systems, e.g. the HydroBalancer HB 6000 [37] or the M6000 system [38]. To be able to dose fluid masses below 1 mg at high spindle speeds, the concept is realized using microfluidic components. With energy supply, controls and communication integrated on the rotor, the system may be used in completely automated procedures.

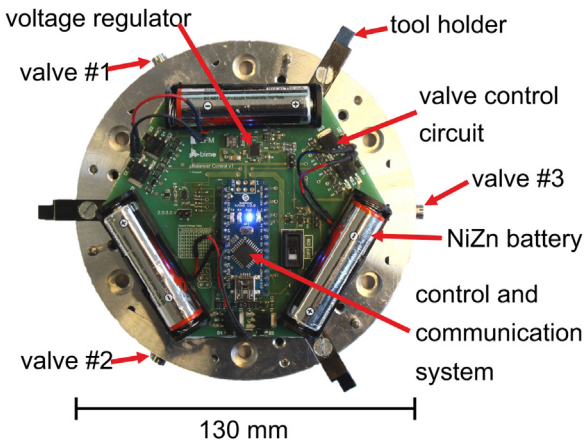

Fig. 7. Automatic microfluidic balancing system with integrated energy supply, control system and electromagnetic valves.

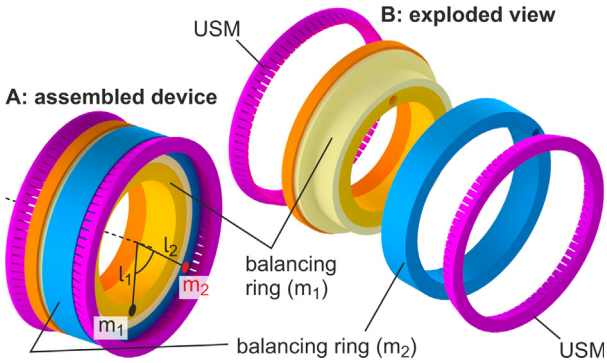

Fig. 8. Rotatory redistribution of masses concept: (a) front view; (b) details of the implemented concept; (c) assembled motors and balancing rings.

Fig. 8 shows the second balancing system with ultra-sonic motors (USM) and balancing rings. In principle, the multiplication of the masses and their distances to the center should be the same (Eq. (4)) [39]:

$$l_1 \cdot m_1 \approx l_2 \cdot m_2 \tag{4}$$

When the system is completely balanced, these masses are located in 180° to neutralize their effects. When an unbalance is detected in the system, the position of masses is changed in a way to compensate the centrifugal force caused by the unbalances (see Section "Balancing capability").

Coupling system

Automated balancing procedures for diamond machining require a fast and precise measurement of unbalances. However, the resulting vibrations of small unbalances are below the detection threshold of common acceleration sensors. Therefore, a coupling system was developed which creates a variable connection between the air bearing spindle and the machine base. This enables the modification of the system stiffness to amplify the unbalance induced vibrations [40].

The coupling system setup is presented in Fig. 9. The top and bottom plates are connected with coupling and flexure joints. These connections ensure high stiffness between the spindle and the spindle housing (machining state). To amplify the unbalances of the system in *X*-direction, the coupling joints are disconnected from the top plates (measuring state).

Experimental setup

The verification of the balancing capability of the automated microfluidic balancing system was carried out on a 4R air bearing spindle from Professional Instruments with a maximum rotational speed of 7500 min^{-1}. For the experiments, a maximum rotational speed of 4800 min^{-1} was chosen to prevent the circuit board from any damage. The rotor unbalance was measured using the balancing measurement system "CAROBA-BALANCER PRO" with high sensitivity acceleration sensors (1000 m V g^{-1}).

Balancing capability

The results of the balancing tests are shown in Fig. 10 as residual unbalance U_{res} compared to the balancing iteration i_{bal}. Each data point in the diagram shows the mean value of three measurements.

The first balancing experiment was conducted at $n = 1500$ min^{-1} (see Fig. 10). This rotational speed was chosen as the measured unbalance is not clearly calculable below this rotational speed and the centrifugal force is not high enough to damage the air bearing. Thereafter, the balancing capability for $n = 2800$ min^{-1} and $n = 4800$ min^{-1} were tested.

The results show a steady decrease of the measured unbalances after each iteration until the threshold is reached. However, the automated balancing system was only able to compensate for the rotor unbalances at the two lower spindle speeds while for $n = 4800$ min^{-1} the system was unable to open the valves due to the higher centrifugal forces. In this case, the spindle was slowed down to $n = 3000$ min^{-1} for balancing and accelerated to 4800 min^{-1} again for measurement. The results indicate that this strategy is feasible as well, as the unbalances are also reduced below the detection limit. In general, balancing at higher spindle speeds requires less iterations than balancing at lower speeds (17 steps at 1500 min^{-1} vs. 7 steps at 4800 min^{-1}).

For testing the improved measurement sensitivity with the coupling system, a three-step balancing procedure was executed, Fig. 11. First, the rigidly connected rotor is balanced until no visible improvement is made near the detection limit. Second, the spindle

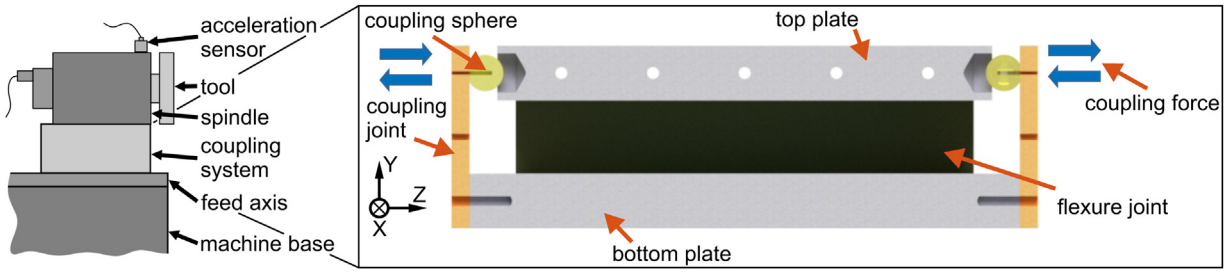

Fig. 9. Side view of coupling system for detection of unbalances.

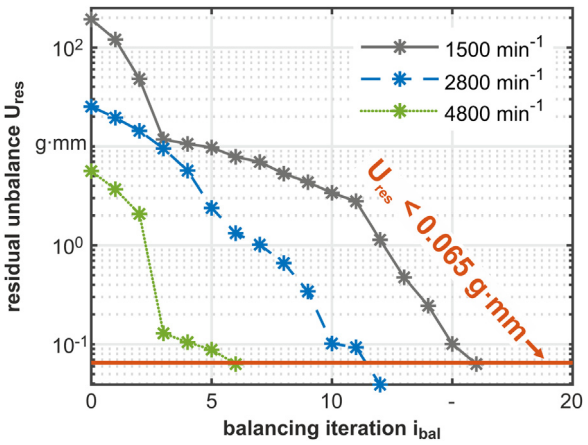

Fig. 10. Measured unbalance during automatic balancing with the microfluidic system for $n = 1500\,\mathrm{min}^{-1}$, $2800\,\mathrm{min}^{-1}$, and $4800\,\mathrm{min}^{-1}$.

is decoupled to increase the vibration magnitude and balancing is conducted again until no vibration is measureable. Third, the spindle is re-coupled and the final balancing state is evaluated.

Comparing the averages of the last seven unbalance measurements before coupling ($U_{res,a} = 0.44 \pm 0.15\,\mathrm{g\,mm}^{-1}$) with the ones after re-coupling ($U_{res,b} = 0.17 \pm 0.06\,\mathrm{g\,mm}^{-1}$) indicates that balancing in the decoupled state improves the balancing state of the rotor. However, the measurements are near the detection level of the sensors.

Improving the efficiency of diamond milling by applying additional cutting edges

The application of multiple cutting edges in a diamond machining process is not trivial due to the required precision ($Sa < 10\,\mathrm{nm}$, $PV < 100\,\mathrm{nm}$). In fact, each milling tool that is added to the setup moves on a slightly different circumference than the others. This difference may be attributed to mechanical tolerances of the tool holder, the cutting insert and also the shape-specifications of the diamond tool. When brought into contact with the workpiece, the radial and axial deviation of the cutting tools cause an irregular surface pattern which cannot be described by a simple formula that takes the feed f, raster spacing s, nose radius r_ε and swing distance r_{fly} into account. Instead, the difference in fly-cut radius Δr_{fly} as well as the difference in axial direction Δs have to be considered. Ultimately, these deviations result in an increased surface roughness compared to fly cutting (Fig. 12).

Tool holder design

Consequently, the application of multiple cutting tools in a milling setup requires a mechanism to align all tools to a common point of engagement. When aiming towards the compensation of deviations in the nanometer range, purely mechanical adjustment is not an option. Therefore, a simplistic approach was considered, based on the utilization of thermal expansion of the tool holders' substrate (see Fig. 13).

The design of a two-tool-holder for diamond milling is presented in [41]. It is made of steel and features two bar-type sections that are irradiated with infrared light from the top and bottom, causing their temperature and thereby their volume to increase, see Table 2 for technical data. By design, the thermal expansion is mainly directed radially, thereby shifting the cutting insert, which is connected to the mechanism, as well.

Ring light for continuous illumination

In order to keep the mass and volume of the rotating tool holder as low as possible, the infrared heat source is kept stationary in the machine tool. Consequently, the time for illuminating the actuator segment is limited when using a single LED. Furthermore, the time in which the actuator is not illuminated/heated is much longer than the heat input. For example, a 30 mm wide actuator at a radius of 60 mm implies that only about 30 mm/(2 ·π· 60 mm), i.e. ≈2/25 of a revolution can be utilized for heating. During the other 23/25, the actuator cools down and shrinks again, causing a deviation of the tool position. To compensate for this, a ring light systems (patent pending) has been developed for quasi-constant illumination of the actuator segment. This allows the heat input to follow the rotation of the tool holder, while the device itself stays stationary.

Tool setting performance

For evaluating the tool setting performance, the step response of the actuator has been measured for the maximum radiant intensity of the LED. The expansion was evaluated by using a capacitive sensor against the circumference of the tool holder at a reference plane below the tool shank (see Fig. 13). All measurements are given as the difference of the respective sections (actuator 1, actuator 2, reference between actuators) to their initial state, i.e. before heating.

In previous investigations, it has been shown that by using the ring light device the actuator is capable of achieving a thermal expansion of $\Delta r \approx 1\,\mu\mathrm{m}$ at a spindle speed of $n = 240\,\mathrm{min}^{-1}$ and an LED-actuator-distance of 10 mm on both sides, cf. [41]. New measurements with an even shorter LED standoff distance of 7 mm

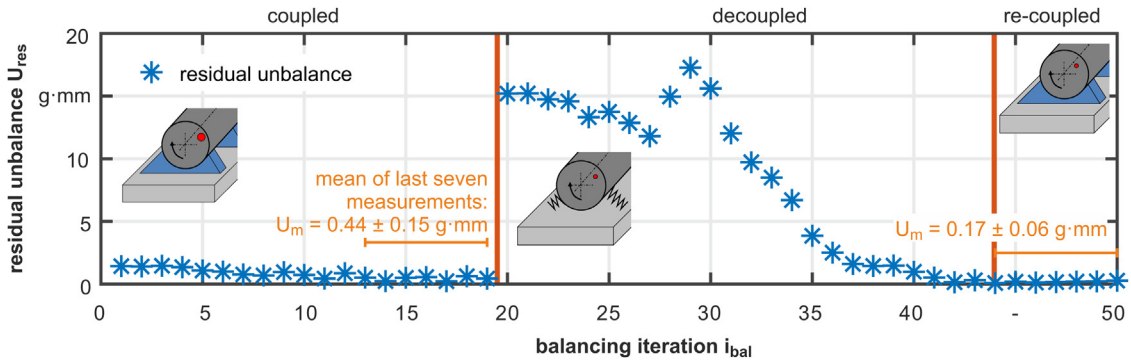

Fig. 11. Balancing procedure by using the coupling system to increase the magnitude of detectable vibrations for increased balancing precision.

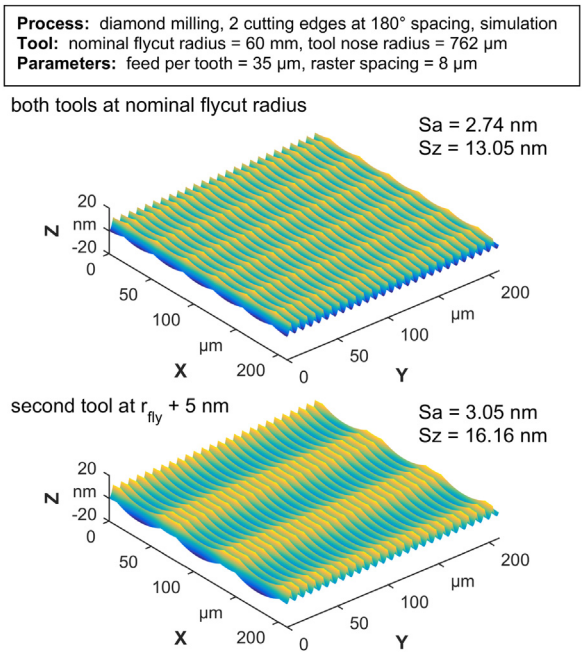

Fig. 12. Simulated surface of a two-tool diamond milling process with and without a deviation in flycut radius.

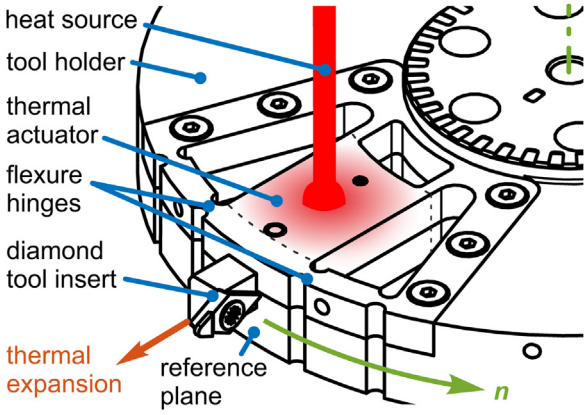

Fig. 13. Principle of a thermal tool holder for generating a radial tool shift by thermal expansion.

Table 2
Technical data of actuator and LED.

Actuator	
Material	steel 1.2083
Thermal conductivity κ	22.6 W m^{-1} K^{-1}
Coef. of thermal expansion α	11.1 µm m^{-1} K^{-1}
dimensions $w \times l \times h$	20 × 25 × 12 mm^3
LED heat source	
Type	Osram SFH-4783
Wavelength λ	850 nm
Half angle φ	±12°
Radiant intensity I_e	2.3 W sr^{-1}
Coef. of thermal absorption η	≈40%

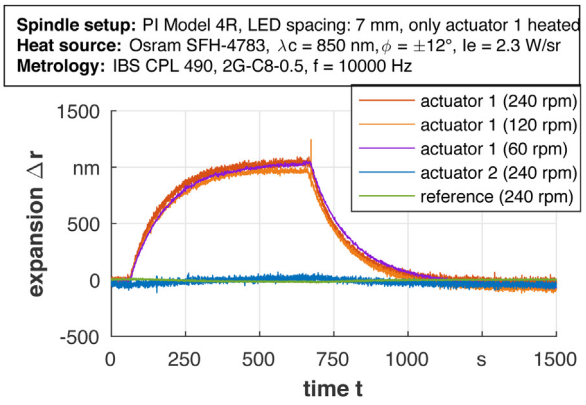

Fig. 14. Thermal expansion of a selectively heated actuator (red), a non-heated actuator (blue) and the reference plane (green) at $n = 240\,\text{min}^{-1}$ and an LED distance of 7 mm as well as expansions of heated actuator at $n = 60\,\text{min}^{-1}$ (violet), $120\,\text{min}^{-1}$ (yellow). (For interpretation of the references to color in this figure legend, the reader is referred to the web version of this article.)

show a similar result (Fig. 14). Furthermore, it has been found that the spindle speed only has a minor influence on the achievable expansion, which in all tested cases ($n = 60\,\text{min}^{-1}$, $120\,\text{min}^{-1}$ and $240\,\text{min}^{-1}$) was around 1 µm, see Fig. 14.

Furthermore, a close-loop control for the actuator position is under development that uses the position of the reference plane as main process variable and controls the LED intensity accordingly.

Impact of tool displacement on unbalance

The change of mass distribution on the tool holder after adjusting the tool position affects the balancing state of the rotor. For the following considerations, it is assumed that the thermal actuator is shifted along with the toolshank and the diamond tool insert in radial direction. Due to the complex geometry of the tool holder, this shift was reproduced in a CAD system, by cutting out the respecting portion and shifting it in radial direction (Fig. 15). The center of mass was calculated by the software before and after the shift and the change in position was calculated afterwards. In total, the radial shift of the center of mass was calculated to 1.2524 µm which is equivalent to a specific unbalance of $e_{p,thermal} = 1.2524\,\text{g mm kg}^{-1}$. This is about 42 times the permissible unbalance of $0.03\,\text{g mm kg}^{-1}$ calculated in Section "Ultra-precision balancing of high speed air bearing spindles" at the maximum spindle speed of $n = 20,000\,\text{min}^{-1}$ and the given rotor weight. Therefore, the thermal actuating mechanism has to be applied with automated balancing procedures, in order to assure a

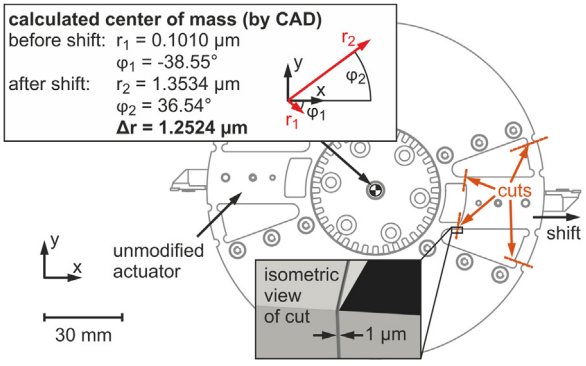

Fig. 15. Calculated change in center of mass when shifting one actuator 1 µm in radial direction.

well-balanced setup at all times. However, it has to be noted that this unbalance is the worst possible scenario, meaning the maximum shifted weight at the highest spindle frequency. For most cases, the thermal expansion and thus the shifted mass will be much smaller ($\Delta r \ll 1\,\mu m$) and the spindle speed significantly slower ($n < 2000\,min^{-1}$), resulting in smaller specific unbalances. Therefore, the actual effect of the thermal actuating mechanism on the unbalance of the rotor has to be evaluated experimentally.

Increasing the feed velocity using electromagnetic levitation technology

Increasing the cutting speed (i.e. spindle speed) and using additional cutting edges require a proportional increase of the feed rate in order to increase the surface generation rate and maintain a consistent chip thickness. Currently, the feed axes of ultra-precision machine tools are designed for the highest possible positioning accuracy. This is often achieved by sacrificing motion dynamics, as high velocity and acceleration tend to increase non-linear friction forces and tilting moments [42]. Moreover, increased acceleration eventually results in higher dynamic errors and excitation of structural vibrations. In this context, the implemented bearing and guide technologies act as major limiting factors due to their finite static stiffness and frequency-dependent properties.

Solution approach and system demonstrator

In view of the current state of the art, the use of electromagnetic levitation technology provides a promising approach to increase the applicable feed rate and acceleration while maintaining the accuracy requirements of ultra-precision machining. The use of electromagnetic actuators enables contactless levitation of moving machine components, thus completely eliminating friction and enabling high feed rates and repeatability. Furthermore, electromagnets offer a high force density and bandwidth which allow for high stiffness and damping. The dynamic properties of electromagnetic guides are significantly influenced by the control system and can be tuned by adjusting the control parameters accordingly [43]. Moreover, the control system allows for the fine positioning of the levitating component within the magnetic air gap. Hence, compensation of static and dynamic errors is feasible.

So far, electromagnetic guides are mainly subject of research projects that cover conventional high-speed cutting [43,44] and high precision positioning [45,46]. However, an electromagnetic linear guide combining nanometer positioning capability and sufficient stiffness for ultra-precision cutting operations has not been presented yet.

A two-axis positioning stage was designed and constructed to investigate the full potential of electromagnetic linear guides in combination with advanced feed axis control techniques. The solution approach to combine high motion dynamics with high precision is to avoid vibration excitation through control measures. Remaining static and dynamic errors are compensated with the electromagnetic guide's fine positioning capability in five degrees of freedom (DoF).

Design of the electromagnetic linear guide prototype

The two-axis stage (depicted in Fig. 16) features a box-in-a-box design. The electromagnetic guide (*X*-axis) is integrated into a movable frame guided by porous media aerostatic bearings (*Z*-axis). Natural granite acts as the main material for the cross table's structural components for its high material damping and low thermal expansion. The travel range of the ironless linear motor driven axes amounts to 100 mm each. invar scales and linear encoders provide position feedback for both axes. Additionally, five capacitive probes measure the orientation and translation of the *Z*-axis in the remaining five degrees of freedom [47]. Fig. 17 shows the basic setup of the new electromagnetic linear guide.

The functional basis of the guide system is a set of reluctance force actuators, each consisting of an electromagnet and a back iron (yoke) [48]. In total, 12 electromagnets in differential arrangement control the guide's five degrees of freedom. Despite the compact core dimensions ($50 \times 25 \times 22.5\,mm$), the electromagnets generate pulling forces of up to 700 N each with a permissible coil current of 12 A. The electromagnets are equipped with capacitive probes (with a dynamic resolution of 2.5 nm at 10 kHz) to measure the magnetic air gap. A set of ironless linear motors in gantry configuration drives the granite slide in feed direction (*X*-direction). With a combined maximum force of 600 N, the direct drives allow for a maximum acceleration of up to $15\,m\,s^{-2}$ for a slide mass of 39.5 kg. The guiding system is designed to reach a velocity of $3000\,mm\,min^{-1}$ over the travel range of 100 mm. An incremental linear scale with a resolution of 1 nm is used as a position encoder in the feed direction.

Furthermore, several measures were implemented to optimize the error budget of the system. The active components of the electromagnetic guide are mounted to the frame to avoid supply lines to the levitating slide as a source of non-linear friction. The electromagnets and linear motors are placed near the slide's horizontal center of gravity plane to minimize cantilevers and

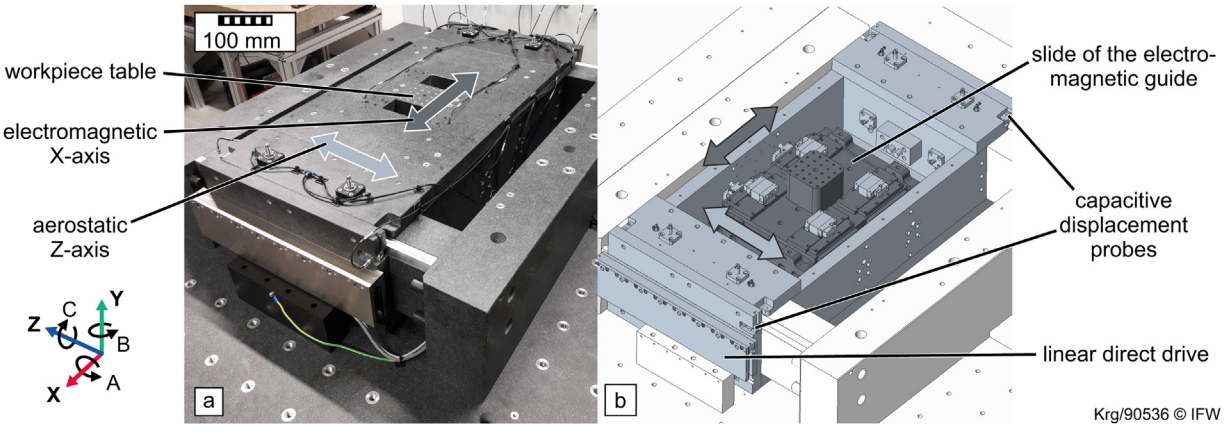

Fig. 16. Ultra-precision two-axis positioning stage.

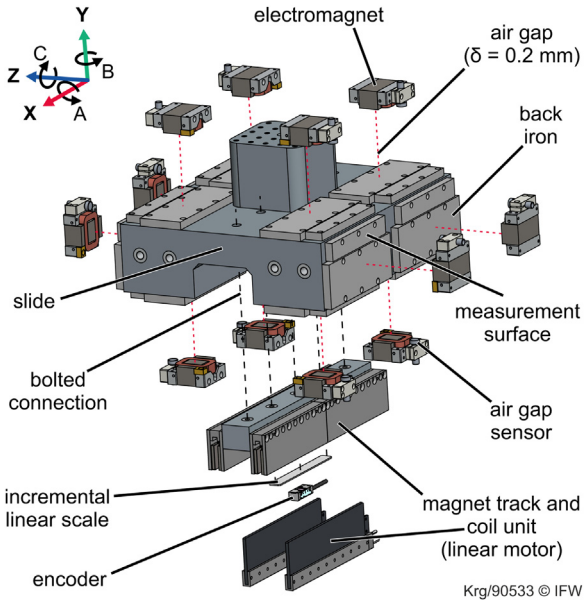

Fig. 17. Setup of the electromagnetic linear guide (exploded view without frame).

unwanted tilting moments. The electromagnets' core geometry and electrical parameters are optimized for a favorable compromise between force dynamics, current ripple and power dissipation [48]. The capacitive measurement system is electrically isolated through glass ceramic sensor holders and grounded measurement targets to minimize sensor noise [49]. The constructed prototype is shown in Fig. 18 (slide) and Fig. 19 (frame with actuators).

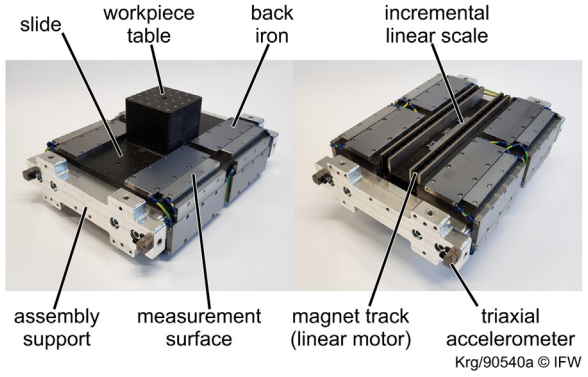

Fig. 18. Granite slide of the constructed test bench.

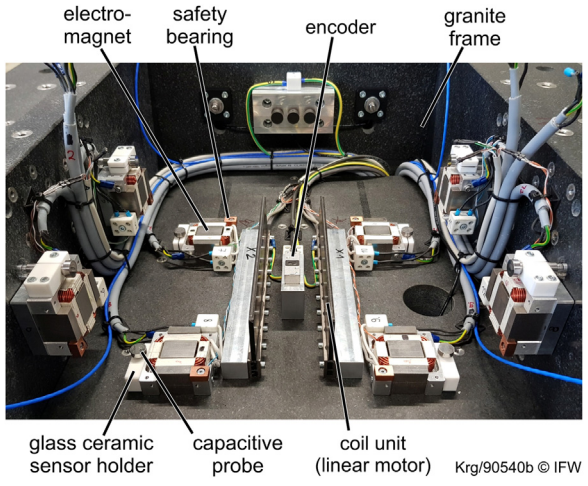

Fig. 19. Open guide frame (without top plate) of the constructed test bench.

Due to the inherently unstable nature of the electromagnetic pulling forces, the electromagnetic guide requires a control system to ensure stable operation. Thus, a control algorithm was designed and implemented in a real-time control environment of an industrial computer. The control algorithm includes the transformation of the 12 air gap signals into five generalized coordinates (according to the two translational and three rotational DoF of the guide) as well as five individual PID controllers for a decoupled DoF control. The hardware connection between industrial computer, power electronics and measurement amplifiers was established via modular terminal systems based on a realtime Ethernet protocol with a sample rate of 20 kHz.

Position accuracy and error compensation

Previous contributions documented the commissioning of the new electromagnetic guide and demonstrated a decoupled control in five degrees of freedom [50]. This work focuses on the (static) characterization of the prototype. For this purpose, the guiding system's position accuracy in all five DoF was measured according to ISO 230-2 using a laser interferometer (with a resolution of 1 nm). The positioning range for the measurement was 50 µm for linear and 400 µrad for rotary movement. Fig. 20 exemplarily illustrates the measurement data for linear movement along the vertical *Y*-axis. Table 3 gives an overview of the complete measurement results.

The measurement data confirms a positioning accuracy in the submicron range. However, the achievable accuracy is limited by the sensor system's noise level, which is considerably affected by the electromagnets and linear motors. In particular, the use of PWM current amplifiers leads to interferences with the capacitive measurement system, which was originally designed for applications in controlled laboratory environments. Varying accuracies in generalized coordinates mainly result from the coordinate transformation, i.e. a different number of sensors per DoF.

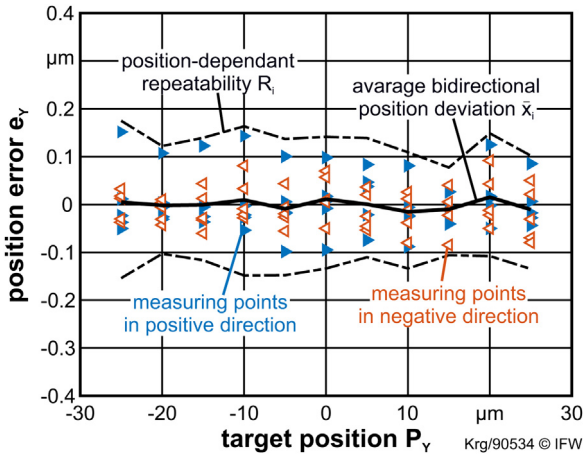

Fig. 20. Position accuracy of the electromagnetic guide in *Y*-direction.

Table 3
Position accuracy of the electromagnetic guide according to ISO 230-2

Measure	Controlled DoF				
	Y µm	*Z* µm	*A* µrad	*B* µrad	*C* µrad
Repeatability *R*	0.25	0.649	3.9	6.4	2.5
Pos. accuracy *A*	0.329	0.712	4.0	7.5	3.1

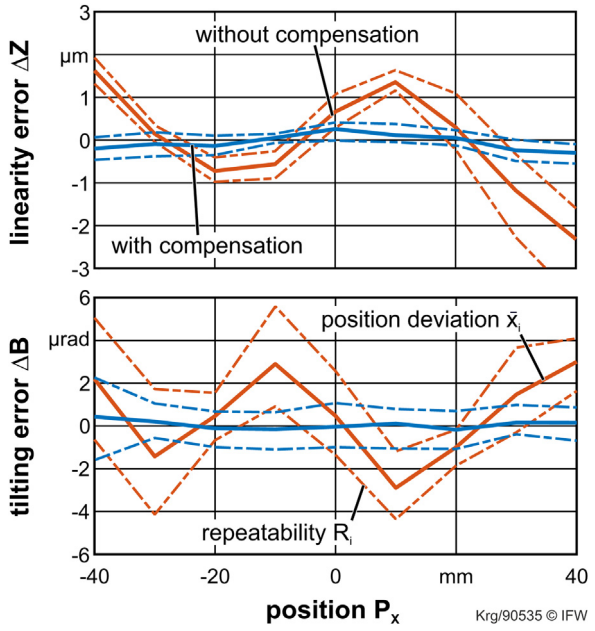

Fig. 21. Compensation of linearity and tilting errors over the travel path (*Z*- and *B*-axis).

In addition to position accuracy, the linearity and tilt errors over the travel path of the electromagnetic guide were determined using a laser interferometer. Fig. 21 illustrates the exemplary measurement results for two of the five error types.

The observed errors result from manufacturing and mounting tolerances of the magnetic yokes and the measurement targets, which cannot be completely avoided in the context of cost-effective production. Since these are systematic errors, they can be effectively compensated with a look-up table. Again, the signal noise of the capacitive measurement system is the limiting factor for the achievable linearity.

Up to now, unfiltered sensor data was used for the calculation of the generalized coordinates and current set-points since the use of filters usually reduces the phase reserve of the closed loop system and destabilizes the controller. On the other hand, the implementation of filter algorithms holds a significant potential to reduce sensor noise and increase position accuracy. Hence, future work will focus on advanced filtering techniques for the electromagnetic guide's control system.

Dedicated UP-HPC control and metrology systems for added performance

Disturbances, which affect control performance, are mitigated by design of the machine as far as possible. This includes the use of ironless linear motors to avoid cogging forces and aerostatic or electromagnetic guides to reduce friction [51,52]. Additionally, in comparison to conventional feed axis position control, signal quality of the position feedback and drive currents affects control performance more strongly. The significant influence of various disturbance effects on ultra-precision machining leads to a high complexity of ultra-precision control systems. Consequently, interdependencies between the subsystems of ultra-precision control systems need to be addressed.

Acceleration of the machine axes can also excite vibrations of the machine structure thereby affecting the machined surface. For UP feed axes decay times of more than two seconds were observed for oscillations following a velocity setpoint change [42]. Thus, reducing decay times is an important part in improving productivity of ultra-precision machining. Common approaches to limit excitation of vibration include the limitation of jerk, acceleration and velocity. However, this harms productivity of the machining process as well. Altintas et al. [53] and Sencer et al. [54] showed that input shaping and frequency optimal trajectory generation can effectively suppress vibration in conventional machining. The feasibility of those approaches was not yet investigated in the context of UP machining.

This research investigates novel control approaches for ultra-precision machining with emphasis methods that allow for higher process productivity and accuracy. The following section focuses on the overall control structure and the modeling of the ultra-precision system.

Control structure

Fig. 22 shows an overview over the control system structure. The control structure of the electromagnetic guide was described in Section “Increasing the feed velocity using electromagnetic levitation technology”. The control loop for the feed drives operates at 16 kHz. Sliding mode control and conventional PPI-cascade control are researched. A Luenberger state observer estimates the feedback for the state control as well as angular deviations of the *Z*-axis. Measured inputs for the observer are the linear encoder values of the *Z*-axis and the values of the capacitive probes. Angular deviations are forwarded to the electromagnetic guide control for compensation. Trajectory generation employs an

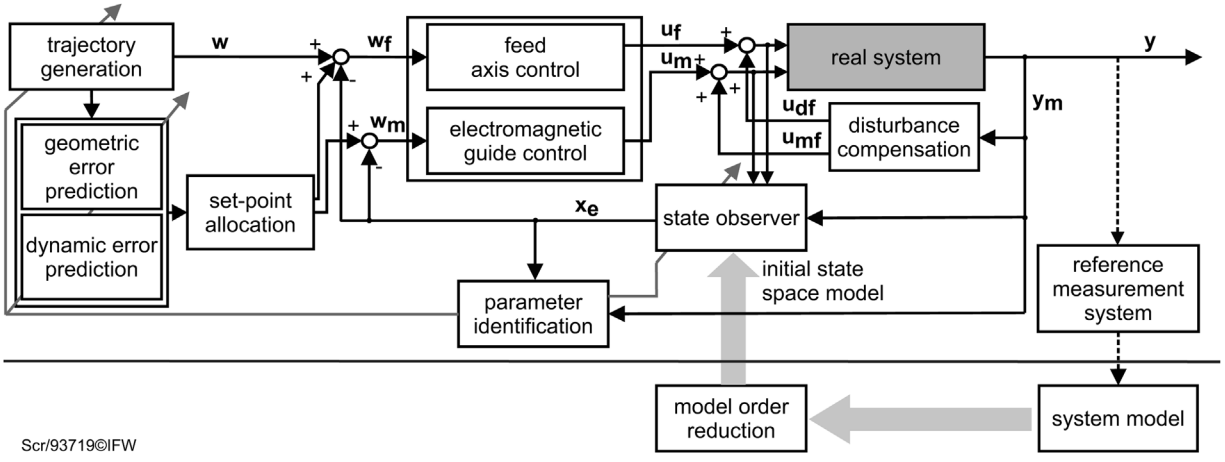

Fig. 22. Overview of the control structure of the ultra-precision system.

input shaping approach to avoid excitation of vibration in order to reduce decay times of the axis and thus increase feasible jerk and acceleration values.

A major challenge for ultra-precision applications are cycle times of the control system. Accurate axis control requires control cycle times to be as low as possible. Accurate and detailed modeling of system dynamics, however, leads to increased cycle times for the calculation of the models. Thus, in order to ensure real-time capability of the complex control system adaptive low order state space models (SSM) are used for error prediction and state observation. The initial SSMs are gained by model order reduction (MOR) of detailed finite element models (FEM). The SSMs for the state observer and dynamic error prediction are continuously updated. The approach for adaptation of the SSM was shown in [55] and validated on a piezo-stage for changing mass parameters.

In order to attenuate influences of disturbance forces, a disturbance feed forward compensation is used. Major disturbance forces result from the energy chain. A force-sensitive mount measures the forces on the *Z*-axis exerted by the energy chain.

Dynamic path and tilt errors are predicted based on the planned trajectory. In combination with prerecorded geometrical errors (Section “Position accuracy and error compensation”), the predicted path errors are allocated to the setpoint values of the *Z*- and *X*-axis as well as the fine-positioning DOFs. Set point allocation to the redundant actuators is based on frequency filtering and direction of the errors.

Modeling of the ultra-precision cross table

In order to gain accurate models for the control system and to research complex interdependencies between the system's components, a detailed finite-element-model of the ultra-precision cross table is developed. The model is described in detail in [47]. The model includes the major components of the ultra-precision cross table. Material parameters of the granite components (density, bulk modulus, and Poisson's ratio) are derived from experimental modal analysis of a single plate of the same material. The aerostatic and electromagnetic bearings are simplified as nonlinear spring-damper elements. For the initial model the manufacturer's stiffness parameters are applied. A damping factor of 0.01 is assumed for the air pads. In the second step, an experimental modal analysis is carried out in order to refine parameters of the FE-model. As the compliance originates largely from the air bearings, their stiffness parameters are refined in a first step. In the next step, the damping values are modified in order to adjust the resonance amplitudes to the measured ones. The damping values are the system's global damping ratio and the local damping values of the mode shapes. Fig. 23 compares the simulated and measured driving point response function in *X*- and *Z*-direction for an excitation on point S. The mode shapes at 97 Hz, 115 Hz and 222 Hz are dominated by a rigid body motion of the *Z*-axis and are in good accordance with the results from the FE-simulation. Especially, the mode at 97 Hz is expected to be excited during motion due to the eccentric load incidence of the linear drives energy chain.

Speckle reference measurement system for evaluating UP control systems

Evaluating the tracking performance of machines is challenging in multiple aspects. One method of evaluating machines is the manufacturing of test parts. Deviations of the test workpiece could be related to the machining process, machine capabilities or elastic deformations due to the clamping of the workpiece. However, the results of this test method are not only related to the feed axes performance [56]. Since the machining time of one ultra-precision test part can take multiple hours, another test method than producing and analyzing a test part is needed to evaluate UP-HPC machines directly.

The axis motions were tracked to analyze the behavior of the ultra-precision control system. This resulted in exceptional challenges on the measurement system. Trajectory tracking had to be evaluated for at least two interpolating feed axes. Conventional measurement systems, like cross-grid meters, do not provide sufficient accuracy for ultra-precision purposes or do not provide acceptable measurement ranges. To respond to these requirements, a speckle-based measurement system was introduced [57].

Laser-speckle occur when an optical rough surface is illuminated by a laser beam. Small defects in the surface cause light interference, i.e. variations of the reflected intensity. As a result of the stochastic distribution of these defects, the reflected light

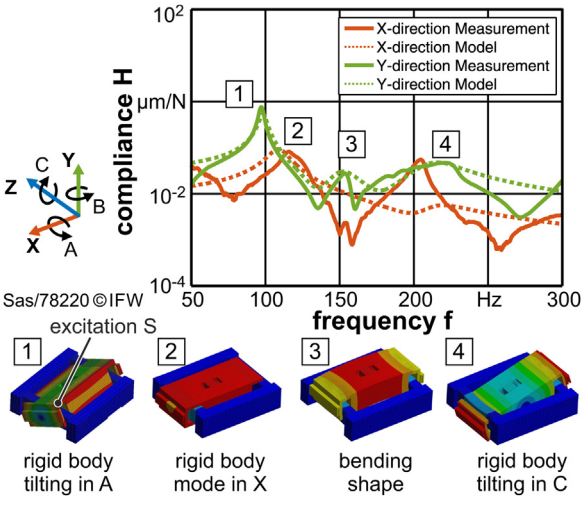

Fig. 23. Structural model of the ultra-precision cross table.

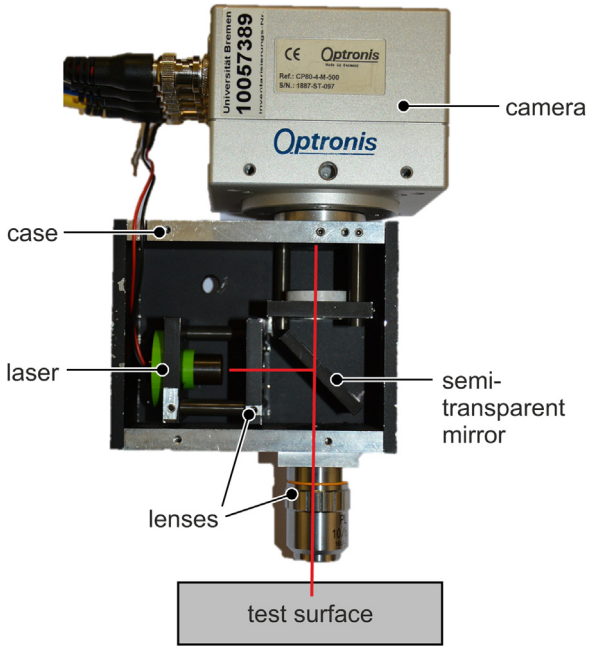

Fig. 24. Experimental setup of the speckle sensor.

creates a unique speckle pattern, which is related to the surface. By tracing the displacement of the speckle pattern, the displacement of the illuminated surface can be calculated. An experimental measurement system was used to measure these displacements of the speckle pattern. The setup is shown in Fig. 24 [58].

To test the axis with this sensor, a multi-scale test path was developed as shown in Fig. 26. The test path included different areas to test different requirements. The horizontal and vertical sections were intended to analyze both feed axis independently. The position accuracy, the acceleration and deceleration and the run into the set point position behavior were determined with these test path sections. The diagonal test path sections were used to test the feed axis in synchronous motion. The circle showed the interaction and interpolation capabilities of the two feed axis. The test path was realized in three different scales. With the different scales, different velocities and ranges could be tested [58].

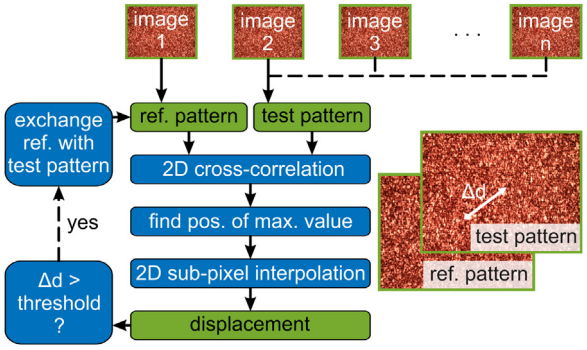

Fig. 25. Algorithm of speckle-based displacement calculation with pattern change.

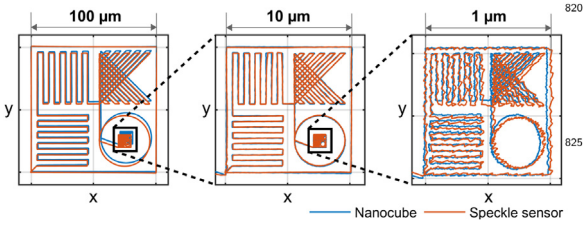

Fig. 26. Results of the speckle based sensor in comparison to the internal position sensors of a piezo based positioning device [58]. (For interpretation of the references to color in this figure legend, the reader is referred to the web version of this article.)

A digital correlation algorithm, shown in Fig. 25, was used to calculate the displacement of the speckle pattern. The algorithm is explained with further details in [57]. The basic idea is that the algorithm calculates the displacement from two pictures. The pattern of the initial image is defined as the reference pattern. This reference pattern represented the position at the beginning of the measurement. The second pattern was defined as the test pattern. This test pattern represented the actual position. In a first step, the displacement of the test pattern is determined by the maximum value of the two-dimensional cross correlation function. The second step is a bi-cubic sub pixel interpolation to increase the resolution. By increasing the displacement, a reduction in overlap between the reference pattern and the test pattern could be seen. When the displacement became larger, the overlap became too small for an accurate image correlation and the reference pattern had to be changed. The timing of this change was evaluated by a threshold value. When the total displacement was larger than the displacement threshold the reference pattern was changed. With every measurement, a small error was unavoidable. With each pattern change, the calculated position of the new reference pattern cumulates this error. Therefore, the threshold value must be high enough to prevent a large amount of changes of reference patterns. Despite this, the threshold must not be too high because of a decreasing accuracy with small overlaps of test pattern and reference pattern [57].

The above described test path was carried out with a Nanocube Piezo Stage P-611.3 (Physik Instrumente). The repeatability of the piezo stage is better than 10 nm and the linearity error is less than 0.1% for each axis. Fig. 26 shows the test pattern measured by the internal position sensor of the Nanocube (blue) and measured by the speckle based sensor (red). The comparison between the two positioning sensors showed on the small scaled test path of 1 µm that the speckle based sensor is able to detect movements in the low nm range. However, with larger patterns, e.g. 100 µm, an increasing error was recorded. This drift should be minimized with advanced referencing technics in further works [58].

Synergistic application of proposed techniques

Every development presented in this paper allows for a significant improvement of a single aspect of ultra-precision milling. The true potential, however, is only achieved if all techniques are used in a combined environment where they are

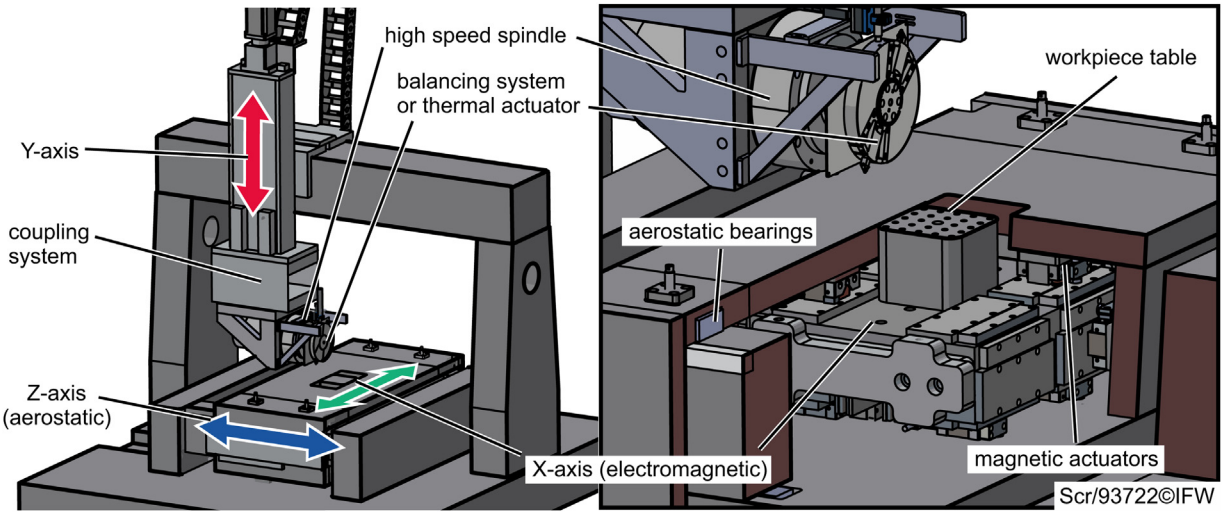

Fig. 27. Concept for the synergistic application of the developments for ultra-precision high performance cutting on a common test stand.

able to supplement each other (Fig. 27). For example, high speed milling alone offers the potential to reduce the cutting forces and allow for longer tool life. But, without viable means to quickly balance the high speed spindle, the machine setup is a tedious and time-consuming process and thus cannot be applied economically. This is similar to the application of multiple diamond cutters on a single milling tool: having more cutting edges engaged in the material process allows for faster movement of the feed axes which, in turn, requires a fast-actuating slide and bearing concept, like the electromagnetic linear guide presented in Section "Increasing the feed velocity using electromagnetic levitation technology". Furthermore, changing the radial position of a cutting edge impacts the balancing state of the rotor and thus has to be counteracted with an automatic balancing system.

Summary and outlook

This paper summarizes the current state of developments of the Research Unit FOR1845 on ultra-precision high performance cutting made by the Universities of Bremen and Hannover over the past years. First, it was shown that high speed cutting does have a positive effect on the material removal and the tool wear in diamond milling, which is explained by the transition to adiabatic shearing. Furthermore, it is shown that with high cutting speed, the ductile machining of brittle-hard materials is facilitated, although the thermal stability of diamond remains a limiting factor, as temperatures above 800 °C are reached in this case.

Thereafter, new mechatronic devices to facilitate the spindle balancing for ultra-precision milling have been introduced, including an automated microfluidic balancer and a rotary system based on ultra-sonic motors. In addition, the residual unbalances of the spindle setup can be amplified by using a coupling system to switch between soft (i.e. amplified unbalances) and rigid connection of the spindle to the machine base. Using these systems, it has been shown that a residual unbalance of $U_{res} < 0,065\,\mathrm{g\,mm}$ is achieved after a few (automated) iterations, i.e. only a few seconds. Nevertheless, for achieving automatic balancing at $n > 3000\mathrm{min}^{-1}$, modifications of the balancing systems and the balancing procedure are still required, to minimize the influence of the centrifugal force.

For further improving the material removal rate, a tool setting mechanism that ultilizes localized thermal expansion has been presented. This is used for precisely setting the tool radius while milling and thereby allows for the application of multiple diamond tools on one tool holder.

On the machine tool side, a novel linear guide based on electromagnetic levitation is presented that allows for fast movements as well as error compensation in five degrees of freedom. It is supplemented by a dedicated control system that applies a model-based structure for prediction and compensation of geometric and dynamic errors. The parameters of the model are continuously identified while the control system is running and updated to the state observer. Furthermore, a speckle sensor system is shown that enables the tracking of complex paths of the cross table by observing speckle pattern.

Acknowledgment

The authors would like to thank the German Research Foundation (DFG) for funding this work as part of the Research Unit FOR 1845 "Ultra-precision High Performance Cutting".

References

[1] Dornfeld, D., Min, S., Takeuchi, Y., 2006, Recent advances in mechanical-micromachining. CIRP Ann, 55/2: 745–768. http://dx.doi.org/10.1016/j.cirp.2006.10.006.
[2] Brecher, C., Lindemann, D., Merz, M., Wenzel, C., Preuss, W., 2013, Freeform machining of molds for replication of plastic optics. in Brinksmeier EE., Gläbe RR., Riemer OO., (Eds.) Fabrication of complex optical components, lecture notes in production engineering. Springer, pp. pp.41–52.
[3] Davies, M.A., Dutterer, B.S., Suleski, T.J., Silny, J.F., Kim, E.D., 2012, Diamond machining of diffraction gratings for imaging spectrometers. Precis Eng, 36/2: 334–338. http://dx.doi.org/10.1016/j.precisioneng.2011.09.006.
[4] Wang, S.J., To, S., Chen, X., Chen, X.D., Ouyang, X.B., 2014, An integrated optimization of cutting parameters and tool path generation in ultraprecision raster milling. Int J Adv Manuf Technol, 75/9–12: 1711–1721. http://dx.doi.org/10.1007/s00170-014-6254-0.
[5] Brinksmeier, E., Preuss, W., 2012, Micro-machining. Philos Trans R Soc A, 370:3973–3992. http://dx.doi.org/10.1098/rsta.2011.0056.
[6] Paul, E., Evans, C.J., Mangamelli, A., McGlauflin, M.L., Polvani, R.S., 1996, Chemical aspects of tool wear in single point diamond turning. Precis Eng, 18/1: 4–19. http://dx.doi.org/10.1016/0141-6359(95)00019-4.
[7] Moriwaki, T., Shamoto, E., 1991, Ultraprecision diamond turning of stainless steel by applying ultrasonic vibration. CIRP Ann, 40/1: 559–562. http://dx.doi.org/10.1016/S0007-8506(07)62053-8.
[8] Brinksmeier, E., Gläbe, R., Osmer, J., 2006, Ultra-precision diamond cutting of steel molds. CIRP Ann, 55/1: 551–554. http://dx.doi.org/10.1016/S0007-8506(07)60480-6.
[9] Takasu, S., Masuda, M., Nishiguchi, T., Kobayashi, A., 1985, Influence of study vibration with small amplitude upon surface roughness in diamond machining. CIRP Ann, 34/1: 463–467. http://dx.doi.org/10.1016/S0007-8506(07)61812-5.
[10] Zhang, S.J., To, S., 2013, The effects of spindle vibration on surface generation in ultra-precision raster milling. Int J Mach Tools Manuf, 71:52–56. http://dx.doi.org/10.1016/j.ijmachtools.2013.04.005.
[11] Liu, X., Zhang, X., Fang, F.Z., Liu, S., 2016, Identification and compensation of main machining errors on surface form accuracy in ultra-precision diamond turning. Int J Mach Tools Manuf, 105:45–57. http://dx.doi.org/10.1016/j.ijmachtools.2016.03.001.
[12] Owen, J.D., Shultz, J.A., Suleski, T.J., Davies, M.A., 2017, Error correction methodology for ultra-precision three-axis milling of freeform optics. CIRP Ann, 66/1: 97–100. http://dx.doi.org/10.1016/j.cirp.2017.04.031.
[13] Zhang, X., Li, Z., Zhang, G., 2018, High performance ultra-precision turning of large-aspect-ratio rectangular freeform optics. CIRP Ann, 67/1: 543–546. http://dx.doi.org/10.1016/j.cirp.2018.04.073.
[14] Zhang, S.J., To, S., Zhu, Z.W., Zhang, G.Q., 2016, A review of fly cutting applied to surface generation in ultra-precision machining. Int J Mach Tools Manuf, 103:13–27. http://dx.doi.org/10.1016/j.ijmachtools.2016.01.001.
[15] Cheng, M.N., Cheung, C.F., Lee, W.B., To, S., Kong, L.B., 2008, Theoretical and experimental analysis of nano-surface generation in ultra-precision raster milling. Int J Mach Tools Manuf, 48/10: 1090–1102. http://dx.doi.org/10.1016/j.ijmachtools.2008.02.006.
[16] Wu, Y., Peng, W., Liu, Y., 2013, A novel fabrication method for micro optical waveguide mold based on fly-cutting technology. Optik – Int J Light Electron Opt, 124/9: 867–869. http://dx.doi.org/10.1016/j.ijleo.2012.02.020.
[17] Kong, L.B., Cheung, C.F., To, S., Lee, W.B., 2009, An investigation into surface generation in ultra-precision raster milling. J Mater Process Technol, 209/8: 4178–4185. http://dx.doi.org/10.1016/j.jmatprotec.2008.11.002.
[18] Knapp, B., Arneson, D., Oss, D., Liebers, M., Vallance, R., Marsh, E., 2011, The importance of spindle balancing for the machining of freeform optics. ASPE spring topical meeting, vol. 51 (ASPE, Raleigh, NC), pp.74–78.
[19] Huang, P., Lee, W.B., Chan, C.Y., 2015, Investigation of the effects of spindle unbalance induced error motion on machining accuracy in ultra-precision diamond turning. Int J Mach Tools Manuf, 94:48–56. http://dx.doi.org/10.1016/j.ijmachtools.2015.04.007.
[20] Brandt, C., Krause, A., Niebsch, J., Vehmeyer, J., Brinksmeier, E., Maaß, P., et al, 2013, Surface generation process with consideration of the balancing state in diamond machining. in Denkena BB., Hollmann FF., (Eds.) Process machine interactions, lecture notes in production engineering. Springer, pp. pp.329–360.
[21] Dewes, R.C., Aspinwall, D.K., 1997, A review of ultra high speed milling of hardened steels. J Mater Process Technol, 69/1–3: 1–17. http://dx.doi.org/10.1016/S0924-0136(96)00042-8.
[22] Schulz, H., Moriwaki, T., 1992, High-speed machining. CIRP Ann, 41/2: 637–643. http://dx.doi.org/10.1016/S0007-8506(07)63250-8.
[23] Jahanmir, S., 2011, Surface integrity in ultrahigh speed micromachining. Proc Eng, 19:156–161. http://dx.doi.org/10.1016/j.proeng.2011.11.095.
[24] Grejda, R., Marsh, E., Vallance, R., 2005, Techniques for calibrating spindles with nanometer error motion. Precis Eng, 29/1: 113–123. http://dx.doi.org/10.1016/j.precisioneng.2004.05.003.
[25] Brinksmeier, E., Gläbe, R., Krause, A., 2007, Precision balancing in ultraprecision diamond machining. in Thornett EE., (Ed.) Laser metrology and machine performance VIII. euspen, pp. pp.262–269.
[26] Brinksmeier, E., Preuss, W., Riemer, O., Rentsch, R., 2017, Cutting forces, tool wear and surface finish in high speed diamond machining. Precis Eng, 49:293–304. http://dx.doi.org/10.1016/j.precisioneng.2017.02.018.
[27] Bifano, T.G., Dow, T.A., Scattergood, R.O., 1991, Ductile-regime grinding: a new technology for machining brittle materials. J Eng Ind, 113/2: 184. http://dx.doi.org/10.1115/1.2899676.
[28] Arif, M., Rahman, M., San, W.Y., 2011, Analytical model to determine the critical feed per edge for ductile-brittle transition in milling process of brittle materials. Int J Mach Tools Manuf, 51/3: 170–181. http://dx.doi.org/10.1016/j.ijmachtools.2010.12.003.

[29] Arif, M., Rahman, M., San, W.Y., 2012, Analytical model to determine the critical conditions for the modes of material removal in the milling process of brittle material. J Mater Process Technol, 212/9: 1925–1933. http://dx.doi.org/10.1016/j.jmatprotec.2012.04.014.
[30] Owen, J.D., Troutman, J.R., Harriman, T.A., Zare, A., Wang, Y.Q., Lucca, D.A., et al, 2016, The mechanics of milling of germanium for IR applications. CIRP Ann, 65/1: 109–112. http://dx.doi.org/10.1016/j.cirp.2016.04.076.
[31] Chen, N., Chen, M., Wu, C., Guo, Y., Wang, Y., 2016, The design and optimization of micro polycrystalline diamond ball end mill for repairing micro-defects on the surface of KDP crystal. Precis Eng, 43:345–355. http://dx.doi.org/10.1016/j.precisioneng.2015.08.015.
[32] Vandeperre, L.J., Giuliani, F., Lloyd, S.J., Clegg, W.J., 2007, The hardness of silicon and germanium. Acta Mater, 55/18: 6307–6315. http://dx.doi.org/10.1016/j.actamat.2007.07.036.
[33] ISO. 2017, Mechanical vibration – rotor balancing – part 11: procedures and tolerances for rotors with rigid behaviour..
[34] Levicron GmbH. 2017, Coorporate website.http://levicron.com.
[35] Dörgeloh, T., Riemer, O., Brinksmeier, E., 2018, Automated microfluidic balancing system for high speed air-bearing spindles. Proc CIRP, 77:263–266. http://dx.doi.org/10.1016/j.procir.2018.09.011. 8th CIRP conference on high performance cutting (HP, 2018).
[36] Foremny, E., Schenck, C., Kuhfuss, B., 2016, Integrated ultrasonic driven balancer for ultra precision high speed machine tools. Proc Technol, 26:316–323. http://dx.doi.org/10.1016/j.protcy.2016.08.041. 3rd international conference on system-integrated intelligence: new challenges for product and production engineering.
[37] Hofman Precision Balancing Ltd. HydroBalancer HB 6000. http://www.hofmann-balancing.co.uk.
[38] Dittel Messtechnik GmbH. Product brochure – balancing heads/AE-sensors/electronics/condition monitoring. http://www.dittel.com.
[39] Dörgeloh, T., Beinhauer, A., Riemer, O., Brinksmeier, E., 2016, Microfluidic balancing concepts for ultraprecision high speed applications. Proc CIRP, 46:185–188. http://dx.doi.org/10.1016/j.procir.2016.03.174. 7th CIRP conference on high performance cutting (HP, 2016).
[40] Foremny, E., Schenck, C., Kuhfuss, B., 2016, Coupling system for ultra precision machining. J Mech Eng Autom, 6/6: 301–306. http://dx.doi.org/10.17265/2159-5275/2016.06.006.
[41] Schönemann, L., Riemer, O., 2018, Thermo-mechanical tool setting mechanism for ultra-precision milling with multiple cutting edges. Precis Eng, 55:171–178. http://dx.doi.org/10.1016/j.precisioneng.2018.09.003.
[42] Bloem, A., Schenck, C., Kuhfuss, B., 2016, Dynamic behavior of ultra precision feed axis at increased velocities. Proc CIRP, 46:456–459. http://dx.doi.org/10.1016/j.procir.2016.04.040.
[43] Denkena, B., Gümmer, O., Flöter, F., 2014, Evaluation of electromagnetic guides in machines tools. CIRP Ann, 63/1: 357–360.
[44] Denkena, B., Kallage, F., Ruskowski, M., Popp, K., Tönshoff, H.-K., 2004, Machine tool with active magnetic guides. CIRP Ann, 53/1: 333–336. http://dx.doi.org/10.1016/S0007-8506(07)60710-0.
[45] Laro, D., 2009, Mechatronic design of an electromagnetically levitated linear position system using novel multi-dof acuators (PhD thesis).Delft University of Technology, Netherlands.
[46] Lu, X., Dyck, M., Altintas, Y., 2015, Magnetically levitated six degree of freedom rotary table. CIRP Ann, 64/1: 353–356. http://dx.doi.org/10.1016/j.cirp.2015.04.107.
[47] Denkena, B., Dahlmann, D., Sassi, N., 2017, Analysis of an ultra-precision positioning system and parametrization of its structural model for error compensation. Proc CIRP, 62:335–339.
[48] Denkena, B., Dahlmann, D., Krüger, R., 2016, Design and optimisation of an electromagnetic linear guide for ultra-precision high performance cutting. Proc CIRP, 46:147–150.
[49] Denkena, B., Bergmann, B., Krüger, R., 2018, Enabling electromagnetic levitation technology for ultra-precision high performance machining. 18th EUSPEN international conference & exhibition, 161–162.
[50] Denkena, B., Dahlmann, D., Krüger, R., 2017, Experimental investigation of an electromagnetic linear guide for ultra-precision high performance machining. 17th EUSPEN international conference & exhibition, 447.
[51] Erkorkmaz, K., Gorniak, J.M., Gordon, D.J., 2010, Precision machine tool X - Y stage utilizing a planar air bearing arrangement. CIRP Ann, 59/1: 425–428. http://dx.doi.org/10.1016/j.cirp.2010.03.086.
[52] Xi, J., Dong, Z., Liu, P., Ding, H., 2017, Modeling and identification of iron-less PMLSM end effects for reducing ultra-low-velocity fluctuations of ultra-precision air bearing linear motion stage. Precis Eng, 49:92–103. http://dx.doi.org/10.1016/j.precisioneng.2017.01.016.
[53] Altintas, Y., Khoshdarregi, M.R., 2012, Contour error control of cnc machine tools with vibration avoidance. CIRP Ann, 61/1: 335–338. http://dx.doi.org/10.1016/j.cirp.2012.03.132.
[54] Sencer, B., Dumanli, A., Yamada, Y., 2018, Spline interpolation with optimal frequency spectrum for vibration avoidance. CIRP Ann, 67/1: 377–380. http://dx.doi.org/10.1016/j.cirp.2018.03.002.
[55] Bloem, A., Schenck, C., Kuhfuss, B., 2016, Adaptive state-space model for ultra-precision feed axis. Proc Technol, 26:20–26. http://dx.doi.org/10.1016/j.protcy.2016.08.004.
[56] Ramesh, R., Mannan, M.A., Poo, A.N., 2000, Error compensation in machine tools – a review. Int J Mach Tools Manuf, 40/9: 1235–1256. http://dx.doi.org/10.1016/s0890-6955(00)00009-2.
[57] Bloem, A., Schenck, C., Kuhfuss, B., 2015, 2D position sensor based on speckle correlation. in Annoni MM., Fassi II., Wiens GG.J.J, Dimov SS., (Eds.) 4M/ICOMM 2015. Milan, Italy, pp. pp.541–544.
[58] Bloem, A., Wilhelmi, P., Schenck, C., Kuhfuss, B., 2016, 2D position sensor based on speckle correlation - experimental setup for high-speed measurements and in field tests. 11th international conference on micro manufacturing (Irvine/CA, USA, paper no. 17), .